PREPRINT DISCLAIMER

This manuscript is a non-peer reviewed preprint submitted to EarthArXiv (https://eartharxiv.org).

This version of the manuscript has been accepted for publication in Geomorphology. The final manuscript can be found at this link: https://doi.org/10.1016/j.geomorph.2025.110076

Please feel free to contact any of the authors; we welcome feedback and suggestions.

Document History

Document History	ocument History						
Version	Date	Action					
		Submitted to EarthArXiv and					
1.0	[2025-05-21]	Earth and Planetary Science					
		Letters					
1.0	[2025-06-01]	Submitted to Geomorphology					
2.0	[2025 10 24]	Accepted for publication in					
	[2025-10-24]	Geomorphology					

Paleo extreme storm waves in the North Atlantic: geological evidence from Sal Island, Cape Verde Archipelago.

A. Rovere^{1,2*}, G. Scicchitano^{4,5}C., E. Casella¹, G. Scardino^{4,5}, C. Barile^{3,4}, G. Vieira⁶, N.A.K. Nandasena⁷, D. D. Ryan³, P. Scussolini⁸, R. S. Ramalho^{9,10}

^{1*}Department for Environmental Sciences, Informatics and Statistics, Ca' Foscari University of Venice, Via Torino 155, Venice, 30172, Italy.

²MARUM - Center for Marine Environmental Sciences, University of Bremen, Leobener Str. 8, Bremen, 28359, Germany.

³Department for Earth Sciences, University of Pisa, Via Santa Maria, 53, 56126 Pisa, Italy. ⁴Department of Earth and Geo-Environmental Sciences, University of Bari Aldo Moro, Via Orabona 4, Bari, 70125, Italy.

⁵Interdepartmental Research Center for Coastal Dynamics, University of Bari Aldo Moro, Via Orabona 4, Bari, 70125, Italy.

⁶Centre of Geographical Studies, Institute of Geography and Spatial Planning - IGOT, University of Lisbon, Portugal.

⁷Civil and Environmental Engineering Department, United Arab Emirates University, Al Ain, 15551, United Arab Emirates.

⁸Institute for Environmental Studies (IVM), De Boelelaan 1111, 1081 Vrije Universiteit Amsterdam, Amsterdam, The Netherlands.

⁹School of Earth and Environmental Sciences, Cardiff University, Park Place, Cardiff, CF10 3AT, UK.
 ¹⁰Instituto Dom Luiz (IDL), Faculdade de Ciências, Universidade de Lisboa, 1749-016 Lisboa, Portugal.

ABSTRACT

The northwestern coast of Sal Island (Cape Verde Archipelago) is characterized by a rocky shoreline that is regularly impacted by Atlantic swells exceeding 4 m in height and 20 s in period. Yet, the only significant geomorphic expression of wave action is an extensive boulder ridge situated atop a rocky cliff, up to 80–100 m inland and between 10 and 15 m above present sea level. The presence of meterscale boulders within this ridge raises a key question: is it actively shaped by modern storm waves, or is it a relic of paleo storms, impacting the shoreline during an interglacial period when sea level was significantly higher than today? To test this hypothesis, we apply a multidisciplinary approach combining satellite and drone imagery, topographic analysis, hydrodynamic modeling, and empirical boulder transport thresholds. Our results show that under current conditions, storm waves do not reach the ridge and cannot generate sufficient flow to mobilize its largest boulders. However, under modeled higher sea-level scenarios exceeding +5 m, wave runup reaches the ridge, and flow velocities are sufficient to initiate boulder transport by sliding and overturning. We therefore conclude that the ridge is a relict feature, most likely emplaced during Marine Isotope Stage 5e, when relative sea level in Sal Island was 5-7 meters higher than today.

Keywords: Extreme waves, Paleo extreme storms, Boulder ridge, Sal Island, Cape Verde

INTRODUCTION

The study of sea storms affecting global coasts within Earth's geological past has the potential to shed light on the impacts that future changes on extreme storms frequency, intensity and direction might have on coastal environments. The study of paleo storms falls under the field of paleotempestology (Muller et al., 2017), which is relatively well-developed only for the most recent geological past, namely the Holocene (Minamidate and Goto, 2024). For this period, several geological proxies formed by extreme waves allow reconstructing past wave climate in different regions, enabling scientists to link observations from paleotempestology proxies to long-term and broad-scale climate patterns (Donnelly and Woodruff, 2007).

There are three main broad categories of direct geological proxies of extreme waves onshore: overwash deposits or deposits in coastal karst basins (e.g., in blue holes), beach ridges, and coastal boulder deposits (Minamidate and Goto, 2024). Typically, studies seek to identify the anomalous occurrence of high-energy sedimentary facies within low-energy ones (Engelhart et al., 2019), and aim at quantifying either the intensity of extreme events (Rodysill et al., 2020) or the recurrence intervals of extreme events in time (Schmitt et al., 2025) from sedimentological or morphological elements characterizing these proxies, often in combination with models of different nature that can provide bounds on coastal inundation or wave flow velocity (Nandasena et al., 2022).

The use of direct wave proxies to study paleo coastal storms is subject to two main challenges. The first is of methodological nature and resides in the fact that high-energy coastal events might be overprinted by non-climatic events such as tsunamis, leading to possible misinterpretations (Marriner et al., 2017). Also, the quantitative assessment of some proxies might rely on assumptions and approaches that are, by nature, prone to errors and uncertainties (Cox et al., 2020). The second challenge is related to the preservation of pristine direct wave proxies in coastal environments, which are among the most energetic on the planet. For this reason, while Holocene storms have been studied at hundreds of sites globally (Minamidate and Goto, 2024), proxies of coastal storms occurred during other Pleistocene interglacials are very rare.

One of the most debated lines of evidence of Pleistocene waves are the large boulders and chevron ridges occurring in Bermuda and the Bahamas (Hearty, 1997; Hearty et al., 1998; Hearty and Tormey, 2017), which were attributed to "superstorms" occurring during the Last Interglacial (125 ka, Hansen et al., 2016), exceeding in intensity those recorded in the historical times. However, the scientific debate has been intense over both the wave energy required to emplace the boulders (Hearty and Tormey, 2017; Rovere et al., 2018, 2017) and over the processes responsible for the emplacement of boulders and chevron ridges (Mylroie, 2018, 2008; Vimpere et al., 2021). On Santa Maria Island, in the Azores, the comparison between modern and Pleistocene boulders yielded contrasting results between sites, hindering the possibility to study paleo wave dynamics in this area (Ávila et al., 2020). In the At Monterey Bay, California, sedimentary structures imprinted on the Santa Cruz marine terrace were used to investigate paleo wave climate (Dupré, 1984). Southern Hemisphere, the Pleistocene strandplain known as Remarkable Banks (Robbins Island, Tasmania), was used to gather information on paleo wave climate (Goodwin et al., 2023) and provided observational evidence that there was, in the mid-to-late MIS 5e (126-119 ka), a poleward shift of ~5° of the westerly storm tracks.

Besides the five locations mentioned above, there are virtually no other sites where direct proxies have been studied in the attempt of reconstructing Pleistocene wave climate. In this paper, we describe a boulder ridge located on the northwestern coast of Sal Island, Cape Verde Archipelago (Atlantic Ocean). We use aerial imagery from both satellite and Unpiloted Aircraft Vehicles (UAV), hydrodynamic models, and empirical formulas for incipient motion of boulders to test the hypothesis that the formation of the ridge was only possible under higher-than-present sea-level conditions, and hence that the genesis of this boulder ridge is to be referred to a former interglacial.

GEOLOGICAL AND HYDRODYNAMIC CONTEXT

Sal is the oldest of the Cape Verde Islands, a mid-plate volcanic archipelago located 600–900 km off the western coast of continental Africa, between 15° and 17° N latitude. With a complex geological history, Sal has experienced a long but episodic magmatic evolution, marked by multiple phases of emergence and submergence since its initial formation in the Early to Mid Miocene. Today, the island represents a deeply eroded volcanic edifice, its relief largely flattened by marine erosion and

subsequently uplifted above sea level through a slow Quaternary tectonic trend (Ramalho, 2011, 2010; Ramalho et al., 2010). As a result, Sal is a low and relatively flat island, characterized by extensive raised Pleistocene marine terraces—many containing consolidated carbonate beach deposits—arranged in staircase-like sequences reaching elevations up to 100 m above present sea level (Lecointre, 1965, 1962; Silva and Torres, 1990; Zazo et al., 2010, 2007). This stepped morphology is especially prominent in the northern part of the island, where a flat, barren platform at ~20 m elevation is punctuated by a few volcanic cones formed during the island's final rejuvenated magmatic stage (1.06–0.6 Ma; Holm et al., 2008; Ramalho, 2011). Here, the coast is rugged and rocky, defined by plunging cliffs made up of horizontally layered basaltic lava flows and cemented calcarenites. Among these, a prominent Mid-Pleistocene marine terrace—composed of fossiliferous limestones—stands close to the cliff edge at 10–15 m above present sea level (Reeb et al., 2024).

Sal belongs to the "Ilhas do Barlavento" or "Windward Islands" of the Cape Verde Archipelago, which are directly exposed to North Atlantic swells. Along its northern coast, wave conditions are energetic year-round, with a mean significant wave height of ~1.8 m and average peak period of ~10 s (Figure 1A), punctuated by extreme swell events exceeding 4 m in height and 20 s in period. These wave conditions have left a striking geomorphic imprint: a prominent boulder ridge situated 10–15 m above present sea level along much of the northern and western coasts (Figure 1B,C). This ridge, up to 130 m wide and located 100–150 m inland from the modern shoreline, consists of clasts with diverse lithologies—including basalts and marine limestones—and a wide size range, from decimeter-scale cobbles to boulders several meters in diameter. These clasts were likely quarried and deposited by waves acting on either the volcanic bedrock or the Mid-Pleistocene limestone platform (Figure 1C).

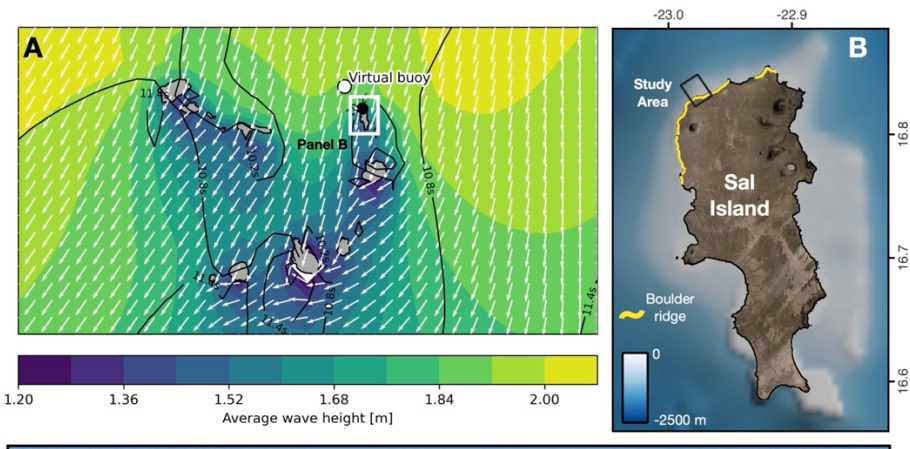




Figure 1. Study area. A) The Cape Verde Archipelago, with average significant wave height (colored contours), peak period (black contours with labels) and wave direction (arrows) extracted from the Copernicus Marine Environment Monitoring Service WAVeReanalYSis (Lellouche et al., 2018) for the period 1980-2024. "Virtual Buoy" indicates the point of extraction of wave data used as hydrodynamic boundary conditions for the hydrodynamic models used in this work. B) Map of Sal Island showing the boulder ridge extent on the North and West coasts (yellow line) and location of the study area, including hydrodynamic

modelling domain. Sources: Orthophotomap of Sal Island at 40 cm resolution. Unidade de Coordenação do Cadastro Predial (UCCP) do Ministério do Ambiente Habitação e Ordenamento do Território (MAHOT). Cape Verde (2010). Bathymetry from GEBCO Compilation Group (2022) GEBCO_2022 Grid (doi:10.5285/e0f0bb80-ab44-2739-e053-6c86abc0289c) C) Drone picture showing the boulder ridge along the northwest coast of Sal Island.

METHODS

High resolution Orthomosaics and Digital Terrain Models

We used aerial images acquired from UAS analyzed with Structure-from-Motion / Multi View Stereo (SfM/MVS) techniques to obtain Digital Terrain Models and Orthomosaics of a site in the northern part of Sal Island. The UAV data was acquired with two different aerial systems in November and December 2019. The aerial images were georeferenced using ground control points measured with differential Global Navigation Satellite Systems (GNSS). As for this area there are no high-accuracy geoid data to refer GNSS ellipsoid data to MSL, DTMs were referred to mean sea level subtracting 30.8551 m from the ITRF 2014 ellipsoid, as per the benchmark sheet of the Permanent Service for Mean Sea Level of the PALMEIRA tide gauge in Sal Island (Station ID 1914) and available levelling data (Donal and Poyard, 2015).

The first UAV survey was done on November 27th, 2019. We used a quadcopter DJI MAVIC PRO drone set on an automated "double grid" path via the "Pix4d Capture" app. We used Agisoft Metashape 2.1.3 to process more than 2700 images divided in three chunks (that were aligned after the calculation of the dense point cloud), each georeferenced to real-world easting, northing and orthometric height coordinates with seven Ground Control Points (GCPs) measured with a pair of EMLID RS+ GNSS configured as Rover-Base, with precise positioning obtained processing the base data with data from the CAP-VERT Espargos GNSS Station (IGS ID: CPGV, with RINEX data retrieved from SONEL, https://www.sonel.org/?page=gps&idStation=3597). The area covered in the November 2019 survey is ~14 ha.

The second UAV survey was conducted between December 18th and 19th, 2019, less than one month after the previous one, using a eBee Plus RTK in PPK mode, equipped with a Sensefly SODA Camera with 20 MP of resolution. A lateral overlap of 70% and longitudinal overlap of 60% were used. A Trimble R4 Base station in static mode was installed in the flight area for post-processing. The base station coordinates were obtained using the Precision Point Positioning Service from Natural Resources Canada and projected in WGS84 UTM Zone 27N, with ellipsoid heights corresponding to ITRF 14 (2019.9).

To assess the differences between the two DTMs, we used the software Cloud Compare. First, we coregistered the two DTMs in the Z coordinate using 80 coregistration points, identified as no-change points in the two orthomosaics (e.g., areas of bare rock, shrubs or ground that remained unchanged between the two acquisitions). Using the "Finely register already aligned entities" command (RMS difference=10⁻⁵, we aligned the Z coordinates of the December 2019 DTM to the elevation of the November 2019 Z at each coregistration point. In this processing, we did not allow for rotation on and translation on the XYZ axis, only allowing translation on the Z axis. We then used the "Cloud to Cloud distance" tool to calculate the elevation (Z) difference between the December 2019 and the November 2019 DTMs (the latter used as reference).

Satellite data analysis

To identify the satellite images corresponding to the most energetic wave conditions, we first extracted the timestamps from all available multispectral images acquired by Landsat 8, Landsat 9, and Sentinel-2, covering the period from 2013 to 2025. Each timestamp was matched with the closest corresponding record in a wave time series obtained from the Copernicus Marine Environment Monitoring Service (WAVeReanalySis dataset; Lellouche et al., 2018), considering only matches within a two-hour time window. For each image, we extracted the significant wave height (VHM0), peak wave period (VTPK), and mean wave direction (VMDR). We then selected the 25 records with the highest wave heights and the 25 with the highest wave periods, removed duplicates, and retained a final set of 46 satellite images. These selected images were imported into QGIS, where the inland extent of wave reach (whitewater) was manually digitized for each image. After excluding scenes affected by excessive cloud cover, whitewater lines were successfully delineated for 23 images. The image coupled with the highest wave height was retrieved by Landsat 8 at on March 1st, 2018 at 11:51 AM (GMT), corresponding to a wave height of 4.4m

196

197

198

199

212

213

214 215 and a peak wave period of 16.4s with a direction of 327.7° N.

To assess whether any visible morphological changes occurred in the boulder ridge over time, we examined historical aerial imagery available through the Google Earth platform using its historical imagery tool. We identified and extracted high-resolution images spanning multiple years and compared them visually. The timing of each image was matched with offshore wave conditions using data from the Copernicus Marine Environment Monitoring Service WAVeReanalYSis dataset.

Hydrodynamic modelling

To simulate waves breaking in the study area, we employ the hydrodynamic model XBeach (Roelvink et al., 2010). We use the non-hydrostatic mode of XBeach, which allows modelling the propagation and decay of individual waves. To obtain a seamless topo bathymetric map, we interpolated the December 2019 DTM obtained from UAV with digitized bathymetric charts of northern Sal Island (Figure 2A, D-H). For the interpolation, we used the TopoToRaster tool of ArcGIS pro (ESRI), inserting as zero contour the shoreline manually digitized on the orthomosaic from the December 2019 UAV flight. To the shoreline, we imposed a "cliff" contour type to make the transition between onland and sea topography sharper, reproducing the shallow plunging cliff observed in the study area. The result of this operation was a 2 m topo bathymetric DTM of the study area. The DTM was then interpolated onto an irregular grid created with Delft Dashboard (Van Ormondt et al., 2020). The irregular grid was created with a spacing of 2.7 m onshore and 5.5 m offshore (Figure 2B,C). The model extends from ~16 m above sea level to the isobath of -100 m. As the coastline in the study area is rocky and we were not interested in sediment transport, we set the entire model domain as non-erodible. We set the bed friction coefficient (manning value) at 0.04, that is slightly lower than the values used for karstified rocky coasts (Pignatelli et al., 2009). The break formulation used is "roelvink daly", which works best when arbitrary breakpoints are present in the wave propagation field (Daly et al., 2011), that is a common occurrence on rocky coasts. Each model was run for one hour.

The wave boundary conditions (significant wave height, peak wave period, peak direction) were extracted from the Copernicus Marine Environment Monitoring Service WAVeReanalYSis (Lellouche et al., 2018) at a virtual wave buoy located offshore the northern part of Sal Island (WGS84 Latitude/Longitude: 17.1063 / -23.1701 degrees, Figure 1A, Supplementary Figure 1B). We ran XBeach with the boundary conditions shown in

Table 1. We ran a set of ten simulations with the maximum wave height recorded at the virtual buov

and increasing level up to above sea level.	Model ID	Significant Wave Height (m)	Peak Wave period (s)	Wave direction (°N)	Sea level (m)	sea 8 m modern
sea level.	1_Hs5_Tp18_dir338_SL0	5	18	338	0	- One
	2_Hs5_Tp18_dir338_SL1	5	18	338	1	
	3_Hs5_Tp18_dir338_SL2	5	18	338	2	
	4_Hs5_Tp18_dir338_SL3	5	18	338	3	
	5_Hs5_Tp18_dir338_SL4	5	18	338	4	
	6_Hs5_Tp18_dir338_SL5	5	18	338	5	
	7_Hs5_Tp18_dir338_SL6	5	18	338	6	
	8_Hs5_Tp18_dir338_SL7	5	18	338	7	
	9_Hs5_Tp18_dir338_SL8	5	18	338	8	
	0 Hs4p4 Tp16p4 dir327 SL0	4.4	16.4	327	0	

simulation was run with the wave conditions corresponding to the wave height recorded in correspondence with the Landsat 8 imagery taken on March 1st, 2018 at 11:51 AM (GMT).

	Significant	Peak	Wave	Sea
Model ID	Wave	Wave	direction	level
	Height	period	(°N)	(m)

Table 1.

	(m)	(s)		
1_Hs5_Tp18_dir338_SL0	5	18	338	0
2_Hs5_Tp18_dir338_SL1	5	18	338	1
3_Hs5_Tp18_dir338_SL2	5	18	338	2
4_Hs5_Tp18_dir338_SL3	5	18	338	3
5_Hs5_Tp18_dir338_SL4	5	18	338	4
6_Hs5_Tp18_dir338_SL5	5	18	338	5
7_Hs5_Tp18_dir338_SL6	5	18	338	6
8_Hs5_Tp18_dir338_SL7	5	18	338	7
9_Hs5_Tp18_dir338_SL8	5	18	338	8
0_Hs4p4_Tp16p4_dir327_SL0	4.4	16.4	327	0

Hydrodynamic boundary conditions used in the XBeach model runs.

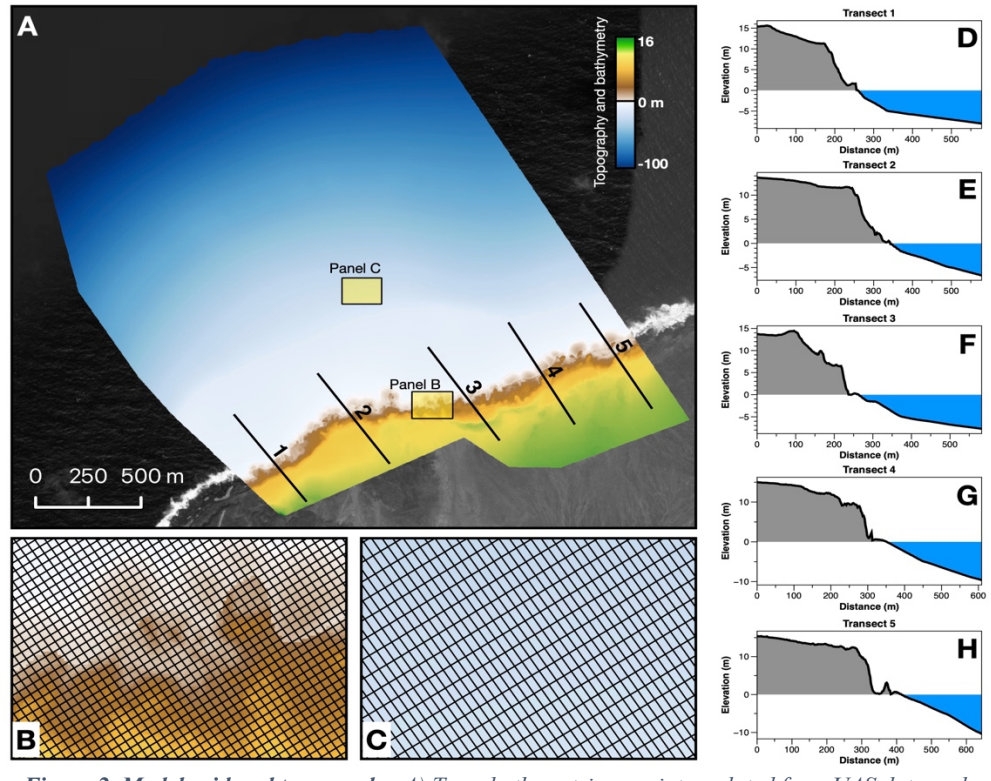


Figure 2. Model grid and topography. A) Topo-bathymetric map interpolated from UAS data and bathymetric charts. B) and C) respectively, grid mesh onshore and offshore. D-H) example of topo-bathymetric transects drawn on the topo-bathymetric map. The image background (grayscale orthophoto) is derived from ESRI World Imagery (Sources: Esri, Maxar, Earthstar Geographics, and the GIS User Community)

Incipient boulder motion

Land-based SfM/MVS methods were used to assess the dimensional parameters of seven coastal boulders located onshore on a limestone outcrop towards the center of the XBeach model domain. Photos of each boulder were acquired at a distance of less than 10 m using a Sony DSC-RX100M3 camera (8.8 mm focal length; 5472 × 3648 resolution). The SfM-MVS processing was carried out in Agisoft Metashape 2.1.3 in order to extract the point clouds representative of boulder dimensional features. Scale bars were used during the SfM/MVS process to scale and optimize the point clouds. Point clouds were then imported into the Cloud Compare software (v.2.13.1) to extrapolate the "ab" and "ac" surfaces

following the approach described by Nandasena et al., 2022 (see Scardino et al., 2025 for a recent application). The surfaces were converted to meshes and translated to planar projections to determine their projected surfaces and axial lengths (a > b > c). Finally, the actual volumes of each boulder were calculated in Cloud Compare. As bulk densities, we used 2300 kg/m³ for limestone boulders, 2500 kg/m³ for boulders with mixed volcanic rock (basalt) and limestones, and 2800 kg/m³ for boulders composed of volcanic rock (basalt). To calculate the minimum flow velocities required to move each boulder, we applied the incipient-motion formulas of Nandasena et al., 2022, using the coefficients shown in Table 2. Among the pre-transport conditions reported in Nandasena et al., 2022, we only calculated threshold flow velocities for submerged or subaerial isolated boulders or joint-bounded boulders, as in the study site we did not survey cliff-edge boulders.

Table 2. Coefficients used to calculate the minimum flow velocity to transport boulders.

Coefficient	Value
Drag	1.5
Lift	0.7
Static Friction	0.5
Bed angle	0.05°

RESULTS

The aim of this work is to test the hypothesis that the boulder ridge located on the northwestern coast of Sal Island was formed under higher sea-level conditions, and it is therefore a relic feature formed by waves during a former interglacial rather than the result of historical wave action. The first step in our hypothesis-testing was to investigate whether historical storm waves can reach the boulder ridge with enough force to modify its morphology. Analyzing the inland reach of the whitewater produced by breaking waves on Landsat 8, 9 and Sentinel 2 images (Supplementary Table 1), we verified that, among the 23 images available taken during days of high wave heights and periods, in none of the images the whitewater reached the boulder ridge (Figure 3A, Supplementary Figure 1A), remaining 80-100 meters far from it in most of the study area. This provides a first confirmation that waves, today, cannot reach the boulder ridge.

Further evidence that historical wave events have not significantly altered the boulder ridge comes from the visual inspection of historical aerial imagery available in Google Earth, dating back to 2005 (Supplementary Figure 2A–L). These images show no visible changes to the morphology of the boulder ridge or displacement of the large boulders, despite the area having been impacted by several major swells during the period analyzed (Supplementary Figure 2M,N). Additional confirmation is provided by the two UAS surveys conducted nearly one month apart (Supplementary Figure 3A,B), a period that included a major swell event with significant wave heights reaching up to 4 m and peak wave periods up to 18 s (Supplementary Figure 3C,D). While field observations revealed some movement of small boulders, sand, and marine litter at the base of the ridge, a comparison between the two high-resolution DTMs indicates only minimal topographic change (Supplementary Figure 3E).

These results suggest that under current sea-level and wave conditions, storm waves are unable to reach or significantly modify the boulder ridge. Therefore, to estimate how much higher sea level must have been during a past interglacial for waves to reach and impact the boulder ridge, we analyzed the outputs of XBeach hydrodynamic simulations run under varying sea-level scenarios. As a preliminary step, we validated the model by comparing the simulated wave runup with the observed inland extent of whitewater in the satellite image acquired during the most energetic storm event captured in the satellite imagery dataset—March 1st, 2018 (Figure 3A, Supplementary Figure 1C, Supplementary Table 1). This validation confirms a close correspondence between the modeled runup and the whitewater reach observed in the imagery (Supplementary Figure 1D), supporting the reliability of the model in reproducing wave behavior under present-day conditions. We then ran a suite of simulations in which

sea level was incrementally raised up to +8 meters relative to present. The results show that wave runup progressively extends further inland with rising sea level: the boulder ridge is first reached when sea level exceeds +5 meters and is fully overtopped by waves at +7 meters (Figure 3B).

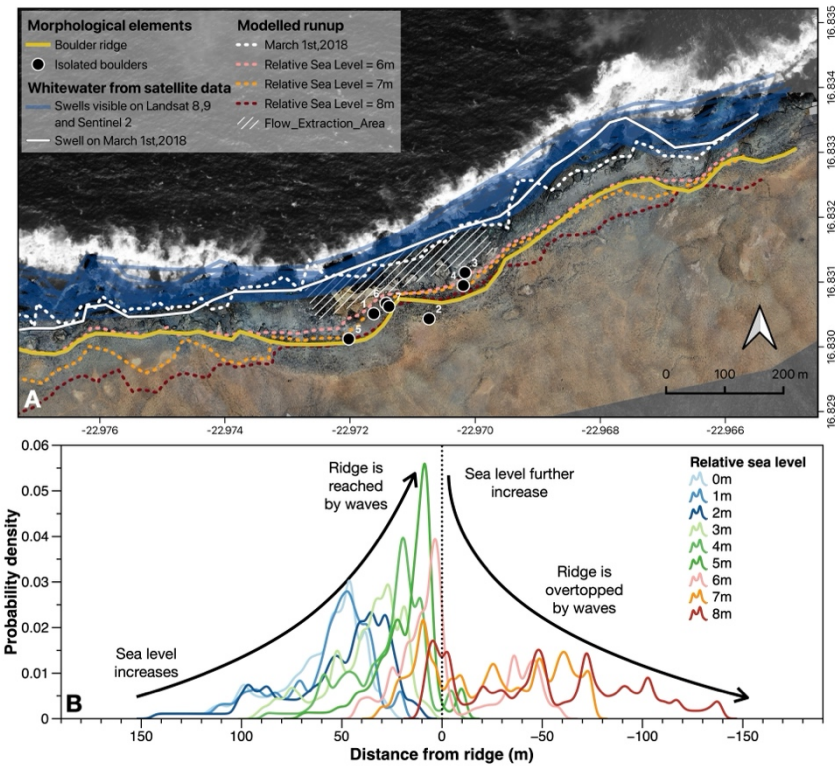


Figure 3. Satellite data analysis and wave modelling. A) Map of the central part of the modelling domain showing: i) reach of waves (whitewater) mapped from satellite data (transparent blue lines) For the same mapping over the complete XBeach modelling domain, see Supplementary Figure 1A; ii) comparison between the whitewater reach of waves during the swell occurred on March 1st, 2018 mapped on the corresponding Landsat 8 image and the runup modelled via XBeach under modern sea level for the same swell (respectively, continuous and dashed white lines); iii) modelled wave runup for the sea level scenarios of 6-7-8 meters (colored dashed lines) and the position of the highest part of the boulder ridge (yellow continuous line). In the panel is also shown the location of the seven isolated large boulders mapped in this work (black dots) and the area where the flow velocity has been extracted from the XBeach model. The image background (grayscale ortophoto) is derived from ESRI World Imagery (Sources: Esri, Maxar, Earthstar Geographics, and the GIS User Community) and from the December 2019 UAS survey (colored ortophoto). B) Distance from the beach ridge reached by wave runup in the XBeach simulations under different sea-level scenarios. Positive values (to the left) indicate that the runup remains seaward of the ridge, while negative values (to the right) indicate that the runup overtops the ridge.

To assess whether wave-driven flow under higher sea-level scenarios could mobilize the largest boulders present in the study area, we first characterized seven representative blocks in terms of size, volume, and density (Supplementary Figure 4). These boulders range in volume from 1.2 to 25.3 m³ and in mass from 3 to 58.2 metric tons (Supplementary Table 2). Their lithology includes pure limestone, volcanic rock (basalts), and composite blocks of limestone embedded with basaltic cobbles. To define the most plausible pre-transport setting for these boulders, we examined the modern coastline, where carbonate blocks are currently being undercut by differential erosion between the more resistant basalt and the softer limestone. This process appears to form structural notches at the base of limestone outcrops, which over time may lead to the detachment and isolation of subaerial boulders, in accordance with the classification of Nandasena et al. (2022). Based on this observation, we adopt the "subaerial/submerged isolated boulder" pre-transport setting in our threshold flow velocity calculations.

Based on this classification, we then compared modeled flow velocities from the XBeach simulations with empirical threshold values for three transport modes relevant to the submerged or subaerial isolated

32.7

pre-transport setting: sliding, overturning, and saltation. Under present-day sea-level conditions, none of the boulders reached the flow thresholds required for any mode of transport, confirming that modern storm waves are insufficient to affect the ridge (Supplementary Table 3). As sea level is progressively raised in the model, all boulders exceed the sliding threshold at relatively modest increases (e.g., +1 to +2 m; Figure 4), while surpassing the overturning threshold requires higher sea levels (e.g., +4 to +5 m; Figure 4). In contrast, the saltation thresholds remain largely unmet across the full range of modeled scenarios. However, in a few cases, modeled flow velocities approach these thresholds—particularly for lighter or more favorably shaped boulders—suggesting that such transport modes could become plausible under even more extreme sea-level rise or more intense wave energy conditions (Figure 4).

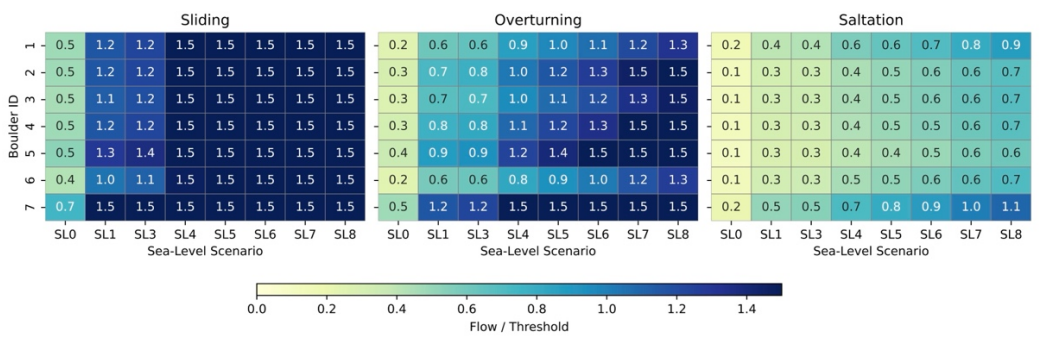


Figure 4. Boulder transport under different sea-level scenarios. Heatmaps showing the relative wave-induced flow intensity experienced by each boulder under different sea-level scenarios for the four transport modes: sliding, overturning, saltation (for submerged or sub-aerial isolated pre-transport setting). Each cell displays the ratio between the maximum modeled flow velocity at the boulder location and the empirical threshold flow velocity required to initiate transport for that specific mode, as defined by Nandasena et al. (2022). Values < 1 indicate that the modeled flow is insufficient to mobilize the boulder. Values \approx 1 suggest the flow is close to the threshold for movement. Values \approx 1 indicate that the boulder could be mobilized under the modeled conditions. For visualization purposes, all values are capped at 1.5. Color intensity reflects proximity to the transport threshold, with darker shades indicating higher modelled flow relative to the required threshold.

DISCUSSION

By integrating satellite imagery, historical aerial photographs, repeat UAS surveys, and wave reanalysis data, we demonstrate that under present sea-level conditions, storm waves on the northwestern coast of Sal Island lack the energy to reach or modify the boulder ridge. The consistent absence of whitewater intrusion across the ridge, the lack of detectable morphological change over nearly two decades of imagery, and the minimal topographic variation captured by high-resolution UAS-derived DTMs all provide multiple, independent lines of evidence pointing to the same conclusion: the ridge has remained stable throughout the historical and modern record. In the absence of continuous in-situ monitoring, this represents the most robust assessment currently achievable for wave impact and coastal stability in the area.

These lines of evidence strongly support the interpretation that the boulder ridge on the northwestern coast of Sal Island is a relict feature, emplaced under sea-level conditions that no longer exist today. Our analysis shows that under present-day conditions, storm waves do not reach the ridge, nor is there evidence of recent morphological change in its structure. Even when sea level is incrementally raised in numerical simulations, wave runup reaches the ridge only when sea level exceeds +5 m, and full overtopping occurs above +7 m relative to present. Importantly, the modeled flow velocities under higher sea-level scenarios are sufficient to exceed the thresholds for boulder transport by sliding and overturning, indicating that movement of even the largest blocks is physically plausible under these conditions. In contrast, saltation—the most energetic and hydrodynamically demanding transport mode—remains largely unattainable across all scenarios, although some boulders approach the necessary thresholds under extreme conditions. On the other hand, the flow depth modeled via XBeach exceeds the height of the c-axis when the sea level surpasses +5 m. These findings suggest that while modern conditions are insufficient to explain the formation or modification of the ridge, it could have been emplaced during a past period of significantly elevated sea level, likely associated with a former interglacial highstand.

While our results strongly support the interpretation of the boulder ridge as a relict feature formed under higher sea-level conditions, several methodological limitations should be acknowledged. First, the XBeach simulations were conducted over a limited portion of the northern Sal Island coastline. Although the study area is representative of the broader ridge morphology, it does not fully capture the spatial variability of coastal topography and wave exposure observed along the entire northern coast. Second, the absence of in-situ wave data—particularly across-shore wave dissipation profiles—precluded a full calibration of the hydrodynamic model. Although the modeled runup closely matched the observed whitewater extent during the March 1st, 2018, storm event, a more robust calibration against empirical measurements would be necessary to reduce uncertainty in the absolute values of modeled flow velocities. Third, our satellite-based analysis is constrained to individual image acquisition times. As such, we cannot rule out the possibility that whitewater may have reached further inland during unsampled moments of storm events, although no persistent evidence of wave impact was detected. Fourth, the wave forcing data used in both the satellite match-up and hydrodynamic modeling were derived from the WAVeReanalYSis product (Lellouche et al., 2018). While this dataset has been validated for accuracy in various settings, it remains a model-based product and may underrepresent the intensity of peak swell events, potentially leading to conservative estimates of wave runup. Lastly, while we based our threshold flow velocity estimates on measured boulder dimensions and well-established empirical equations, uncertainties remain in the exact pre-transport setting, the hydrodynamic exposure of individual clasts, and the topography at the time of transport (which could have been different from the modern topography we used as boundary condition in our models).

Taken together, these limitations suggest that our estimates of the wave conditions required to mobilize the ridge are likely conservative. Nonetheless, the convergence of multiple lines of independent evidence—from satellite data, historical imagery, UAS surveys, and numerical modeling—provides a strong basis for concluding that modern storm conditions are insufficient to explain the emplacement of the ridge. This reinforces the interpretation of the feature as a legacy of past high-energy, high sea-level conditions.

A key question that needs to be answered is which interglacial period may have been responsible for its deposition. Previous studies on the southern coast of Sal Island dated shallow-water marine fauna found at +2.5 m above present sea level to Marine Isotopic Stage (MIS) 5e (Zazo et al., 2007), and correlated Pleistocene limestones on the western and northern coasts, found at +5 to +6 m, to the same interglacial (Zazo et al., 2010, 2007; Reeb et al., 2024). This elevation range is lower than the carbonate buildup at our study site and from which the boulders were likely sourced, which is located at elevations between 10 and 15 m and with its age being attributed to the Mid Pleistocene (775–129 ka), and possibly associated with MIS 11 or MIS 9 (Reeb et al., 2024). This suggests that the boulders were plucked, transported and emplaced during MIS 5e, when local sea level was 5-6 m higher than the present day. Moreover, if deposition had taken place during one of these older interglacials, such an interpretation would require the boulders to have remained in place, unmodified, through subsequent sea-level highstands—most notably MIS 5e. Given the evidence for significant sea-level rise during MIS 5e (locally, at least +5-6m, Zazo et al., 2007), it is more likely that any older deposits would have been reworked during that time. Therefore, the lack of evidence for reworking and the elevation of the source platform both support an MIS 5e origin for the boulder ridge.

The question of whether MIS 5e was characterized by storms more intense than those of the Holocene has long been debated, particularly in the context of boulder ridges and high runup deposits observed in Bermuda and the Bahamas (Hearty, 1997; Hearty et al., 1998; Hearty and Tormey, 2018, 2017; Rovere et al., 2018, 2017). Using numerical models like those employed in the present study, Rovere et al. (2017) challenged the hypothesis that "superstorms" were necessary to explain the emplacement of large boulders during MIS 5e. Their results indicated that elevated sea levels alone could account for the observed inland transport of boulders, without requiring unusually high wave energy. Accepting the hypothesis that the boulder ridge on Sal Island formed during MIS 5e, our results align with this view: the modeled wave runup and flow velocities under elevated sea-level scenarios are sufficient to explain boulder transport without invoking storm conditions more extreme than those occurring today. This is further supported by a comparison of modeled wind fields in the broader study region (Scussolini et al., 2023), which shows that while average wind speeds—those most relevant for slightly lower than those of the present interglacial, the top 10% of wind speeds—those most relevant for

storm-driven wave events—are comparable between the two periods (Figure 5). This suggests that boulder transport during MIS 5e may have occurred under wind-generated swells similar to those of today, but amplified by higher sea levels, rather than by an increase in storm intensity.

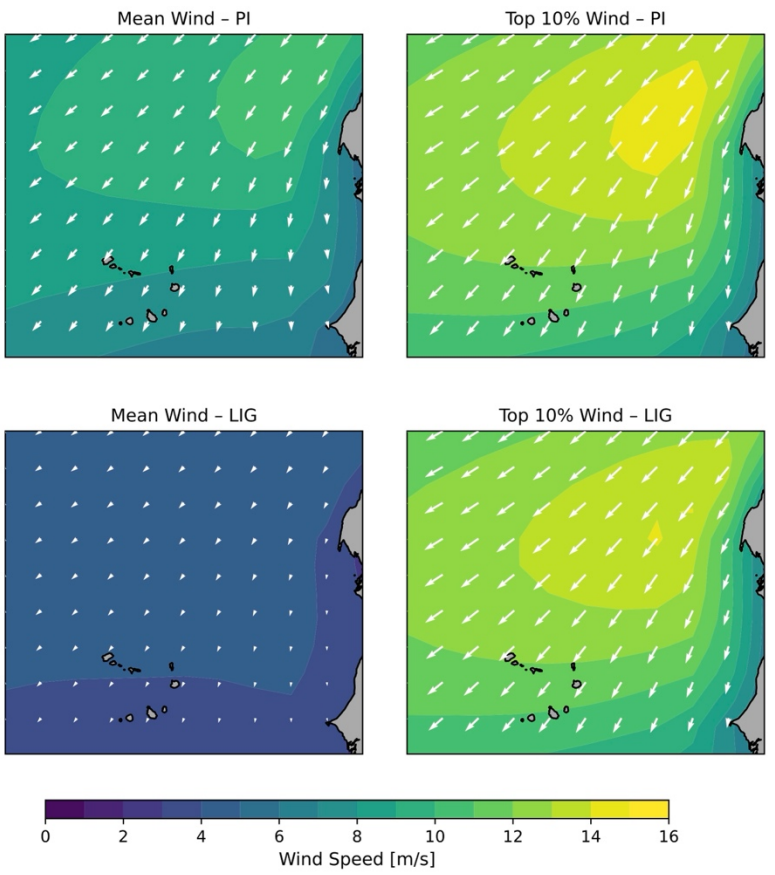


Figure 5. Wind field comparison between the Pre-Industrial (PI) and Last Interglacial (LIG) periods. Data from Scussolini et al. (2023). Left column shows mean wind speed and direction; right column shows the average of the top 10% strongest wind events. Wind vectors indicate direction and relative magnitude.

An open question regarding the boulder ridge on the northern coast of Sal Island is whether its morphology has been modified by one or more paleo-tsunamis following its initial deposition. Certain features of the ridge suggest this possibility. In its northernmost sector, for instance, the ridge becomes unusually wide—extending up to 130 m inland from the seaward edge—and lacks a distinct crest, resembling more a dispersed boulder field than a classic storm-constructed ridge. In addition, isolated large boulders are found significantly inland from the main ridge alignment, which could point to episodic high-energy transport beyond what is typical of storm processes.

These observations might be interpreted as evidence of a tsunami overprint. However, they contrast with the dominant morphological organization observed along most of the ridge, where boulders are arranged in landward-facing cusps aligned with ramp-like erosional corridors carved into the cliff. This kind of repeated and spatially organized pattern is more characteristic of storm-wave activity, consistent with ridge emplacement during a past interglacial highstand—likely MIS 5e.

Nonetheless, a tsunami-related disturbance cannot be entirely ruled out. In particular, the megatsunami generated by the catastrophic flank collapse of Fogo volcano—dated to \sim 68–73 ka—represents a plausible candidate. This event, originating in the southwestern part of the archipelago, is well documented through chaotic boulder deposits and conglomerates on other Cape Verde islands (Costa et al., 2021; Madeira et al., 2020; Paris et al., 2018, 2011; Ramalho et al., 2015). For the resulting wave to affect the northwestern coast of Sal Island, it would have had to travel northward and refract

around Sal Island. Crucially, this collapse occurred during a period of lower sea level (estimated at $-30 \,\mathrm{m}$ to $-80 \,\mathrm{m}$ relative to present, (Gowan et al., 2021; Miller et al., 2011; Spratt and Lisiecki, 2016)), meaning that any wave reaching Sal's coast would have needed considerable height and energy to transport boulders far inland at elevation significantly above relative sea level at the time of transport, a process well documented from field evidence in the more proximal coastlines of the tsunami source (Ramalho et al., 2015).

CONCLUSION

This study tested the hypothesis that the prominent boulder ridge on the northwestern coast of Sal Island was emplaced during a past interglacial, rather than by modern storm activity. Through a multidisciplinary approach—combining satellite and drone imagery, topographic surveys, hydrodynamic modeling, and boulder transport empirical equations—we provide multiple, independent lines of evidence that converge on the same conclusion: under present sea-level conditions, storm waves do not reach the ridge, and no recent morphological change is detectable. Numerical simulations show that the ridge is only reached when sea level is raised above +5 m, and that flow velocities under these scenarios are sufficient to transport even the largest boulders by sliding and overturning. Wind modeling further indicates that the most intense storm events during the Last Interglacial (MIS 5e) were comparable to those of today, suggesting that elevated sea level—rather than extraordinary storm intensity—was the key driver of ridge formation.

While our conclusions are supported by consistent results across methods, limitations remain. These include the restricted spatial extent of the model domain, the absence of in-situ wave calibration data, and the potential underestimation of extreme wave conditions in the reanalysis products. Moreover, a tsunami overprint—particularly from the ~ 70 ka flank collapse of Fogo volcano—cannot be excluded, especially given the inland dispersion of some boulders.

Nonetheless, the dominant morphology of the ridge and the modeling results support a storm-wave origin tied to MIS 5e sea-level conditions. As a well-preserved record of coastal processes during a past highstand, this site offers rare insight into how rising sea levels—even in the absence of stronger storms—can amplify wave-driven coastal hazards. In the context of ongoing climate change, these findings highlight the importance of understanding the interaction between sea level and wave energy in shaping high-energy coasts.

ACKNOWLEDGMENTS

This project has received funding from the European Research Council (ERC) under the European Union's Horizon 2020 research and innovation programme (grant agreement no. 802414 to Alessio Rovere). The manuscript reflects only the view of the authors, and the EU is not responsible for any use that may be made of the information it contains. Fieldwork was also supported by project IF/01641/2015 MEGAWAVE, funded by FCT – Fundação para a Ciência e a Tecnologia I.P. Parts of the data analyses presented in this work were supported by the Marine Science Laboratory of the Department of Earth and Geoenvironmental Sciences at the University of Bari Aldo Moro.

DATA AVAILABILITY

All the data and models used in this study is available via Zenodo at this doi: 10.5281/zenodo.15479905

A preprint of this manuscript was submitted to EarthArXiv and is available at this doi: https://doi.org/10.31223/X58X53

AUTHOR CONTRIBUTION STATEMENT

A. Rovere conceived the MS, was part of the field team and performed satellite and aerial imagery data analysis and wrote the first draft and successive drafts coordinating the input of other co-authors. G. Scicchitano helped streamline the concepts of the paper and contributed substantially to the writing and data analysis. E. Casella, G. Vieira and R.S. Ramalho collected and analyzed UAV data in Cape Verde. G. Scardino, E. Casella, C. Barile and N.A.K. Nandasena worked on defining boulder motion thresholds and XBeach modelling. D.D. Ryan participated to field surveys and worked on the mapping of proxies

of past sea-level highstands in Cape Verde. P. Scussolini worked on paleo wind models. R.S. Ramalho contributed substantially to the writing of the MS and led field data collection and interpretation. NOTE. Portions of the data analysis and figure preparation workflows, including debugging and optimization of Python code, were supported through interactive use of OpenAI's ChatGPT (GPT-4). The tool was also used iteratively under the supervision of the lead author to enhance clarity and structure in the scientific writing process. All interpretations and conclusions were independently developed and validated by the authors.

REFERENCES

484

485 486

487

488

489

490

491

492

493

494

495

496

497

498 499

500

501 502

503

504

505

506 507

508

509

510 511

512513

514

515

516

517

518

519 520

521

522523

524

525

526

527528

- Ávila, S.P., Johnson, M.E., Rebelo, A.C., Baptista, L., Melo, C.S., 2020. Comparison of Modern and Pleistocene (MIS 5e) Coastal Boulder Deposits from Santa Maria Island (Azores Archipelago, NE Atlantic Ocean). J. Mar. Sci. Eng. 8, 386. https://doi.org/10.3390/jmse8060386
- Costa, P.J., Dawson, S., Ramalho, R.S., Engel, M., Dourado, F., Bosnic, I., Andrade, C., 2021. A review on onshore tsunami deposits along the Atlantic coasts. Earth-Sci. Rev. 212, 103441.
- Cox, R., Ardhuin, F., Dias, F., Autret, R., Beisiegel, N., Earlie, C.S., Herterich, J.G., Kennedy, A., Paris, R., Raby, A., Schmitt, P., Weiss, R., 2020. Systematic Review Shows That Work Done by Storm Waves Can Be Misinterpreted as Tsunami-Related Because Commonly Used Hydrodynamic Equations Are Flawed. Front. Mar. Sci. 7, 4. https://doi.org/10.3389/fmars.2020.00004
- Daly, C., Roelvink, D., Van Dongeren, A., Van Thiel De Vries, J., McCall, R., 2011. Short wave breaking effects on low frequency waves. Coast. Eng. Proc. 20. https://doi.org/10.9753/icce.v32.waves.20
- Donal, T., Poyard, J.C., 2015. Sal ITRF local tie survey (No. 28 560). IGN Service de Géodésie et Nivellement.
- Donnelly, J.P., Woodruff, J.D., 2007. Intense hurricane activity over the past 5,000 years controlled by El Niño and the West African monsoon. Nature 447, 465–468. https://doi.org/10.1038/nature05834
- Dupré, W.R., 1984. Reconstruction of paleo-wave conditions during the Late Pleistocene from marine terrace deposits, Monterey Bay, California, in: Developments in Sedimentology. Elsevier, pp. 435–454.
- Engelhart, S.E., Pilarczyk, J.E., Rovere, A., 2019. Storms and extreme events: Insights from the historical and paleo record. Past Glob. Chang. Mag. 27, 2017–2018. https://doi.org/10.22498/pages.27.1.26
- Goodwin, I.D., Mortlock, T.R., Ribo, M., Mitrovica, J.X., O'Leary, M., Williams, R., 2023. Robbins Island: The index site for regional Last Interglacial sea level, wave climate and the subtropical ridge around Bass Strait, Australia. Quat. Sci. Rev. 305, 107996.
- Gowan, E.J., Zhang, X., Khosravi, S., Rovere, A., Stocchi, P., Hughes, A.L.C., Gyllencreutz, R., Mangerud, J., Svendsen, J.I., Lohmann, G., 2021. A new global ice sheet reconstruction for the past 80 000 years. Nat. Commun. 12, 1–9. https://doi.org/10.1038/s41467-021-21469-w
- Hansen, J., Sato, M., Hearty, P., Ruedy, R., Kelley, M., Masson-Delmotte, V., Russell, G., Tselioudis, G., Cao, J., Rignot, E., Velicogna, I., Tormey, B., Donovan, B., Kandiano, E., von Schuckmann, K., Kharecha, P., Legrande, A.N., Bauer, M., Lo, K.-W., 2016. Ice melt, sea level rise and superstorms: evidence from paleoclimate data, climate modeling, and modern observations that 2 °C global warming could be dangerous. Atmospheric Chem. Phys. 16, 3761–3812. https://doi.org/10.5194/acp-16-3761-2016
- Hearty, P.J., 1997. Boulder Deposits from Large Waves during the Last Interglaciation on North Eleuthera Island, Bahamas. Quat. Res. 48, 326–338. https://doi.org/10.1006/qres.1997.1926
- Hearty, P.J., Neumann, A.C., Kaufman, D.S., 1998. Chevron Ridges and Runup Deposits in the Bahamas from Storms Late in Oxygen-Isotope Substage 5e. Quat. Res. 50, 309–322. https://doi.org/10.1006/qres.1998.2006
- Hearty, P.J., Tormey, B.R., 2018. Listen to the whisper of the rocks, telling their ancient story. Proc. Natl. Acad. Sci. 115. https://doi.org/10.1073/pnas.1721253115
- Hearty, P.J., Tormey, B.R., 2017. Sea-level change and superstorms; geologic evidence from the last interglacial (MIS 5e) in the Bahamas and Bermuda offers ominous prospects for a warming Earth. Mar. Geol. 390, 347–365. https://doi.org/10.1016/j.margeo.2017.05.009
- Holm, P.M., Grandvuinet, T., Friis, J., Wilson, J.R., Barker, A.K., Plesner, S., 2008. An 40Ar-39Ar study of the Cape Verde hot spot: Temporal evolution in a semistationary plate environment. J. Geophys. Res. Solid Earth 113.
- 532 Lecointre, G., 1965. Le Quaternaire marin de l'Afrique du nord-ouest. Quaternaria 7, 9–28.
- Lecointre, G., 1962. Le Quaternaire de l'île de Sal (archipel du Cap-Vert). C. r. Somm. Séances Société Géologique Fr. 92– 534 93.
- Lellouche, J.-M., Greiner, E., Le Galloudec, O., Garric, G., Regnier, C., Drevillon, M., Benkiran, M., Testut, C.-E.,
 Bourdalle-Badie, R., Gasparin, F., others, 2018. Recent updates to the Copernicus Marine Service global ocean
 monitoring and forecasting real-time 1/12 deg high-resolution system. Ocean Sci. 14, 1093–1126.
- Madeira, J., Ramalho, R.S., Hoffmann, D.L., Mata, J., Moreira, M., 2020. A geological record of multiple Pleistocene tsunami inundations in an oceanic island: the case of Maio, Cape Verde. Sedimentology 67, 1529–1552.
- Marriner, N., Kaniewski, D., Morhange, C., Flaux, C., Giaime, M., Vacchi, M., Goff, J., 2017. Tsunamis in the geological
 record: Making waves with a cautionary tale from the Mediterranean. Sci. Adv. 3, e1700485.
 https://doi.org/10.1126/sciadv.1700485

- Miller, K.G., MouNtaiN, G.S., WriGht, J.D., BroWNiNG, J.V., 2011. A 180-million-year record of sea level and ice volume variations from continental margin and deep-sea isotopic records. Oceanography 24, 40–53.
- 545 Minamidate, K., Goto, K., 2024. Unveiling the history and nature of paleostorms in the Holocene. Earth-Sci. Rev. 253, 104774. https://doi.org/10.1016/j.earscirev.2024.104774
- Muller, J., Collins, J.M., Gibson, S., Paxton, L., 2017. Recent Advances in the Emerging Field of Paleotempestology, in:
 Collins, J.M., Walsh, K. (Eds.), Hurricanes and Climate Change: Volume 3. Springer International Publishing,
 Cham, pp. 1–33. https://doi.org/10.1007/978-3-319-47594-3
 - Mylroie, J.E., 2018. Superstorms: Comments on Bahamian fenestrae and boulder evidence from the last interglacial. J. Coast. Res. 34, 1471–1483.
 - Mylroie, J.E., 2008. Late Quaternary sea-level position: Evidence from Bahamian carbonate deposition and dissolution cycles. Quat. Int. 183, 61–75. https://doi.org/10.1016/j.quaint.2007.06.030
 - Nandasena, N.A.K., Scicchitano, G., Scardino, G., Milella, M., Piscitelli, A., Mastronuzzi, G., 2022. Boulder displacements along rocky coasts: A new deterministic and theoretical approach to improve incipient motion formulas. Geomorphology 407, 108217. https://doi.org/10.1016/j.geomorph.2022.108217
 - Paris, R., Naylor, L.A., Stephenson, W.J., 2011. Boulders as a signature of storms on rock coasts. Mar. Geol. 283, 1–11. https://doi.org/10.1016/j.margeo.2011.03.016
- Paris, R., Ramalho, R.S., Madeira, J., Ávila, S., May, S.M., Rixhon, G., Engel, M., Brückner, H., Herzog, M., Schukraft, G., others, 2018. Mega-tsunami conglomerates and flank collapses of ocean island volcanoes. Mar. Geol. 395, 168–187.
 - Pignatelli, C., Sansò, P., Mastronuzzi, G., 2009. Evaluation of tsunami flooding using geomorphologic evidence. Mar. Geol. 260, 6–18. https://doi.org/10.1016/j.margeo.2009.01.002
 - Ramalho, R.S., 2011. Building the cape verde Islands. Springer Science & Business Media.

552

553

554555

556

557

558

562563

564

565

566567

568

569

570571

572

573574

575576

577

578

579

580

581

582

583 584

585

586

587 588

589

590

591

592

593

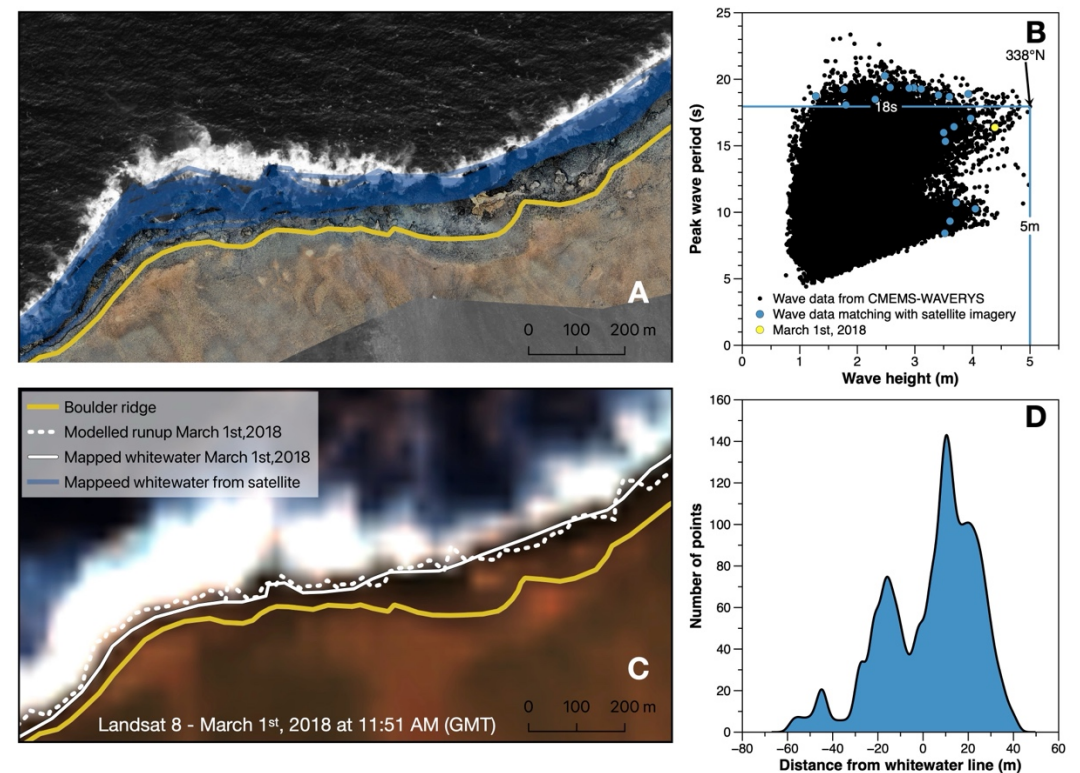
- Ramalho, R.S., 2010. Tracers of Uplift and Subsidence in the Cape Verde Archipelago, in: Building the Cape Verde Islands. Springer Berlin Heidelberg, Berlin, Heidelberg, pp. 79–138. https://doi.org/10.1007/978-3-642-19103-9 5
- Ramalho, R.S., Helffrich, G., Cosca, M., Vance, D., Hoffmann, D., Schmidt, D.N., 2010. Episodic swell growth inferred from variable uplift of the Cape Verde hotspot islands. Nat. Geosci. 3, 774–777.
- Ramalho, R.S., Winckler, G., Madeira, J., Helffrich, G.R., Hipólito, A., Quartau, R., Adena, K., Schaefer, J.M., 2015. Hazard potential of volcanic flank collapses raised by new megatsunami evidence. Sci. Adv. 1, e1500456.
- Reeb, A.-S., Rebelo, A.C., Ramalho, R.S., Madeira, J., Rasser, M.W., 2024. Systematics and paleobiogeography of Quaternary corals from Cabo Verde Archipelago. Quat. Res. 121, 94–108. https://doi.org/10.1017/qua.2024.20
- Rodysill, J.R., Donnelly, J.P., Sullivan, R., Lane, P.D., Toomey, M., Woodruff, J.D., Hawkes, A.D., MacDonald, D., d'Entremont, N., McKeon, K., Wallace, E., Van Hengstum, P.J., 2020. Historically unprecedented Northern Gulf of Mexico hurricane activity from 650 to 1250 CE. Sci. Rep. 10, 19092. https://doi.org/10.1038/s41598-020-75874-0
- Roelvink, D., Reniers, A., Van Dongeren, A., Van Thiel de Vries, J., Lescinski, J., McCall, R., 2010. XBeach model description and manual. Unesco-IHE Inst. Water Educ. Deltares Delft Univ. Techhology Rep. June 21, 2010.
- Rovere, A., Casella, E., Harris, D.L., Lorscheid, T., Nandasena, N.A.K., Dyer, B., Sandstrom, M.R., Stocchi, P., D'Andrea, W.J., Raymo, M.E., 2018. Reply to Hearty and Tormey: Use the scientific method to test geologic hypotheses, because rocks do not whisper. Proc. Natl. Acad. Sci. 115. https://doi.org/10.1073/pnas.1800534115
- Rovere, A., Casella, E., Harris, D.L., Lorscheid, T., Nandasena, N.A.K., Dyer, B., Sandstrom, M.R., Stocchi, P., D'Andrea, W.J., Raymo, M.E., 2017. Giant boulders and Last Interglacial storm intensity in the North Atlantic. Proc. Natl. Acad. Sci. 114, 12144–12149. https://doi.org/10.1073/pnas.1712433114
- Scardino, G., Rovere, A., Barile, C., Nandasena, N.A.K., Chauveau, D., Dahm, M., Boyden, P., Bejarano, S., Casella, E., Kelly, H., Mijts, E., Scicchitano, G., 2025. Coastal boulders emplaced by extreme wave events impacting the ABC islands (Aruba, Bonaire, Curaçao; Leeward Antilles, Caribbean). Quat. Sci. Rev. 349, 109136. https://doi.org/10.1016/j.quascirev.2024.109136
- Schmitt, D., Gischler, E., Melles, M., Wennrich, V., Behling, H., Shumilovskikh, L., Anselmetti, F.S., Vogel, H., Peckmann, J., Birgel, D., 2025. An annually resolved 5700-year storm archive reveals drivers of Caribbean cyclone frequency. Sci. Adv. 11, eads5624. https://doi.org/10.1126/sciadv.ads5624
- Scussolini, P., Dullaart, J., Muis, S., Rovere, A., Bakker, P., Coumou, D., Renssen, H., Ward, P.J., Aerts, J.C., 2023. Modeled storm surge changes in a warmer world: the Last Interglacial. Clim. Past 19, 141–157.
- 595 Silva, L.C., Torres, P.C., 1990. Carta geológica de Cabo Verde: Ilha do Sal. Instituto de investigação científica tropical.
- 596 Spratt, R.M., Lisiecki, L.E., 2016. A Late Pleistocene sea level stack. Clim. Past 12, 1079–1092. https://doi.org/10.5194/cp-597 12-1079-2016
- Van Ormondt, M., Nederhoff, K., van Dongeren, A., 2020. Delft Dashboard: a quick set-up tool for hydrodynamic models.

 J. Hydroinformatics 22, 510–527.
- Vimpere, L., Del Piero, N., Shawwa, N.A., Beguelin, K., Kindler, P., Castelltort, S., 2021. Upper Pleistocene parabolic ridges (i.e. 'chevrons') from the Bahamas: Storm-wave sediments or aeolian deposits? A quantitative approach.
 Sedimentology 68, 1255–1288. https://doi.org/10.1111/sed.12828

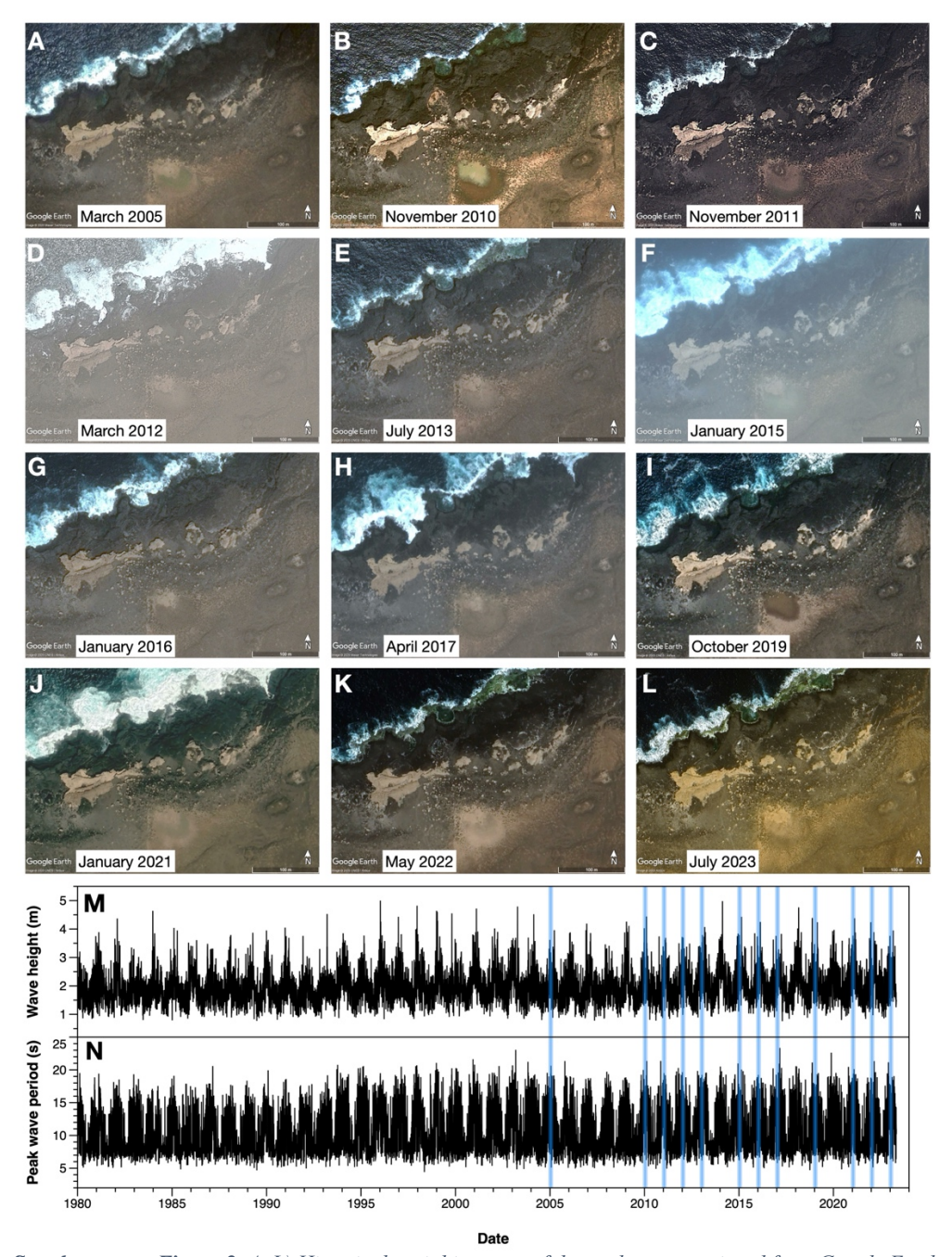
PALEO EXTREME WAVES ON SAL ISLAND, CAPE VERDE ARCHIPELAGO.

603	Zazo, C., Goy, J.L., Dabrio, C.J., Soler, V., Hillaire-Marcel, Cl., Ghaleb, B., Gonzalez-Delgado, J.A., Bardaji, T., Cabero,
604	A., 2007. Quaternary marine terraces on Sal Island (Cape Verde archipelago). Quat. Sci. Rev. 26, 876–893.
605	https://doi.org/10.1016/j.quascirev.2006.12.014
606	Zazo, C., Goy, J.L., Hillaire-Marcel, C., Dabrio, C.J., González-Delgado, J.A., Cabero, A., Bardají, T., Ghaleb, B., Soler,
607	V., 2010. Sea level changes during the last and present interglacials in Sal Island (Cape Verde archipelago). Glob
608	Planet. Change 72, 302–317. https://doi.org/10.1016/j.gloplacha.2010.01.006
609	
610	

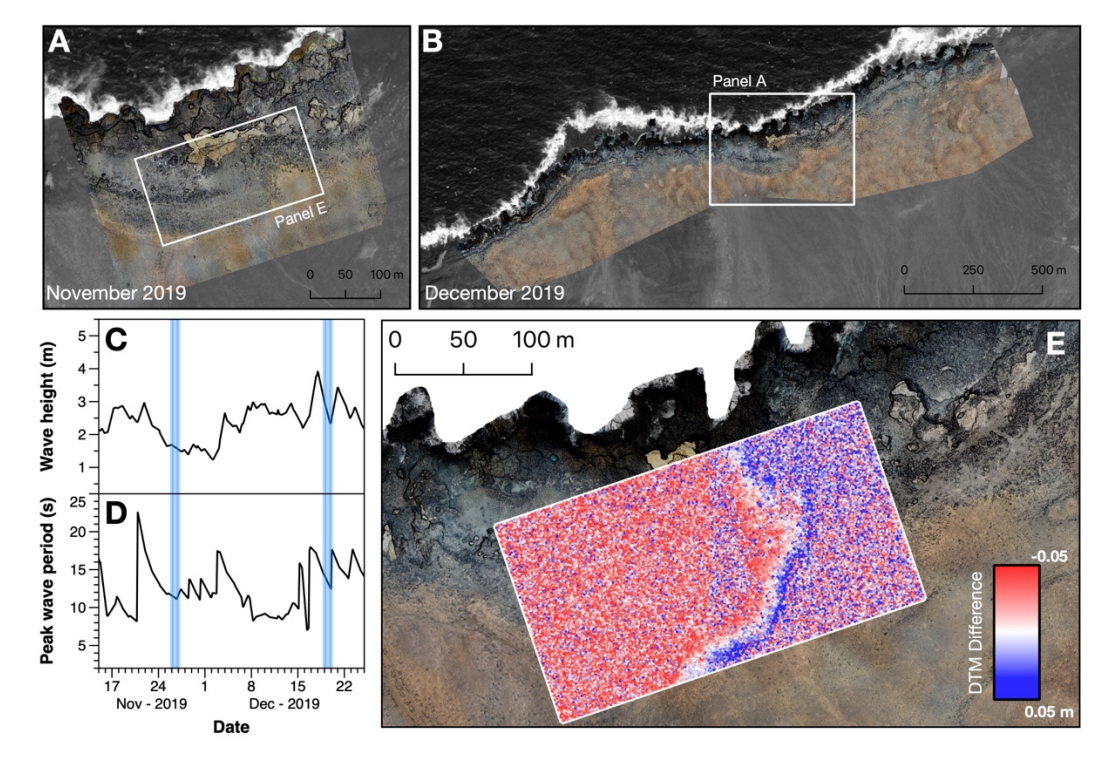
SUPPLEMENTARY FIGURES



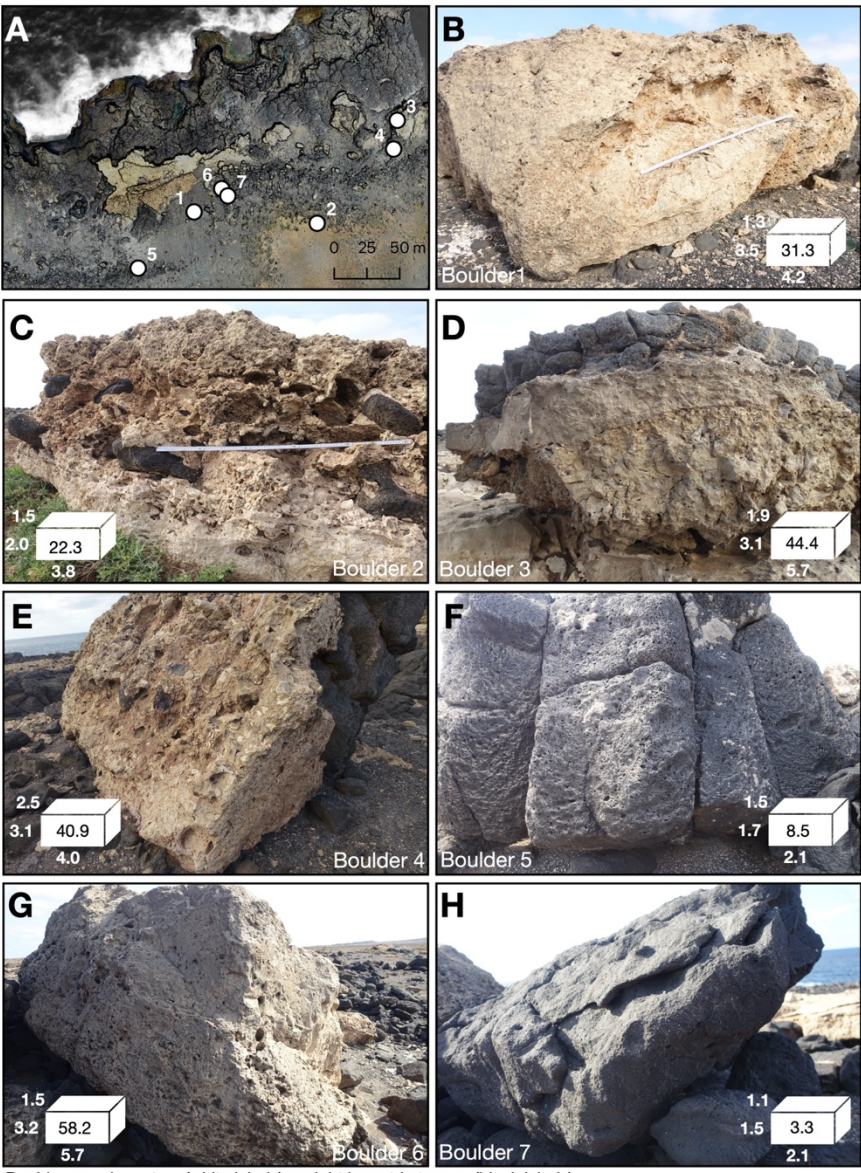
Supplementary Figure 1. A) Reach of whitewater mapped from satellite imagery compared to the position of the ridge over the entire modelling domain. The image background (grayscale ortophoto) is derived from ESRI World Imagery (Sources: Esri, Maxar, Earthstar Geographics, and the GIS User Community) and from the December 2019 UAS survey (colored ortophoto). B) Significant wave height and peak wave period extracted from the Copernicus Marine Environment Monitoring Service WAVeReanalYSis (Lellouche et al., 2018) at a virtual wave buoy located offshore the northern part of Sal Island (WGS84 Latitude/Longitude: 17.1063 /-23.1701 degrees). In the panel are highlighted the wave conditions corresponding to the available satellite images (blue dots) and the wave conditions corresponding to the March 1st, 2018 Landsat 8 imagery. In the image is also indicated the highest significant wave height in the record, alongside with its associated period and direction, which were used in the XBeach modelling. C) Landsat 8 image acquired during a swell on March 8th, 2018, with corresponding mapped whitewater (continuous white line) and modelled runup (dashed white line). D) Distance between the whitewater and the wave runup reached in the XBeach simulations. Positive values (to the left) indicate that the modelled runup underestimates the observed whitewater, while negative values (to the right) indicate that the runup overestimates the observed whitewater.



Supplementary Figure 2. A–L) Historical aerial imagery of the study area retrieved from Google Earth, showing the state of the boulder ridge at different times. M–N) Time series of significant wave height (VHM0) and peak wave period (VTPK), respectively, with blue bands indicating the months during which each historical image was acquired. Wave data were obtained from the Copernicus Marine Environment Monitoring Service WAVeReanalYSis dataset (Lellouche et al., 2018), using a virtual wave buoy positioned offshore of northern Sal Island (WGS84 coordinates: 17.1063° N, 23.1701° W).



Supplementary Figure 3. A–B) Orthomosaics from UAS surveys conducted in November and December 2019, overlaid with hillshade for enhanced topographic visualization. The background in both images is a grayscale orthophoto derived from ESRI World Imagery (Sources: Esri, Maxar, Earthstar Geographics, and the GIS User Community). C–D) Time series of significant wave height and peak wave period recorded between the two UAS surveys. Wave data were obtained from the Copernicus Marine Environment Monitoring Service WAVeReanalySis dataset (Lellouche et al., 2018), using a virtual wave buoy positioned offshore of northern Sal Island (WGS84 coordinates: 17.1063° N, 23.1701° W). E) Topographic difference between the two digital terrain models (DTMs), highlighting changes that occurred over the one-month interval. The background image is the November 2019 UAS orthomosaic.



Boulder axes in meters (white labels), weight in metric tonnes (black labels)

Supplementary Figure 4. Isolated boulders mapped in the study area. A) Location of the boulders. The background image is the November 2019 UAS orthomosaic. B-H) Images, dimensions and weights of the seven boulders mapped in this work.

SUPPLEMENTARY TABLES

Supplementary Table 1. Metadata for the 46 satellite images selected based on matching wave energy conditions. The table reports the image ID, acquisition date and time, significant wave height (VHM0, in meters), peak wave period (VTPK, in seconds), and mean wave direction (VMDR, in degrees from north), along with the time difference (in minutes) between image acquisition and the closest wave data record. The final column indicates whether each image was accepted for whitewater digitization or rejected due to cloud cover or insufficient visibility.

Image ID	Acquisition date and time	VHM0 (m)	VTPK (s)	VMDR (°N)	Time difference (minutes)	Accepted / Rejected
2018-03-01-11-51-29_L8_209049	01/03/18 11:51	4.39	16.38	327.71	8.5	A
2016-02-19-12-06-53_S2_27QTU	19/02/16 12:06	4.05	10.26	24.63	6.9	A
2018-11-19-11-57-30_L8_210048	19/11/18 11:57	3.97	17.06	330.35	2.5	A
2018-11-18-12-16-58_S2_27QTU	18/11/18 12:16	3.93	18.89	331.74	17.0	A
2021-02-27-12-07-08_S2_27QTU	27/02/21 12:07	3.72	10.71	23.07	7.1	A
2015-12-21-12-07-16_S2_27QTU	21/12/15 12:07	3.68	16.43	341.98	7.3	A
2020-01-09-11-57-46_L8_210048	09/01/20 11:57	3.61	9.33	37.92	2.2	A
2020-01-09-12-07-04_S2_27QTU	09/01/20 12:07	3.61	9.33	37.92	7.1	A
2020-10-30-12-07-12_S2_27QTU	30/10/20 12:07	3.6	18.69	13.66	7.2	A
2019-12-18-12-16-59_S2_27QTU	18/12/19 12:16	3.53	15.33	358.15	17.0	A
2021-03-07-12-17-04_S2_27QTU	07/03/21 12:17	3.52	8.43	10.88	17.1	A
2018-04-19-12-06-57_S2_27QTU	19/04/18 12:06	3.5	15.99	344.4	7.0	A
2018-11-10-12-07-06_S2_27QTU	10/11/18 12:07	3.41	18.81	5.42	7.1	A
2022-11-30-11-58-08_L8_210048	30/11/22 11:58	3.11	19.27	335.12	1.9	A
2022-03-12-11-51-45_L8_209049	12/03/22 11:51	2.98	19.37	5.46	8.3	A
2022-03-12-12-17-08_S2_27QTU	12/03/22 12:17	2.98	19.37	5.46	17.1	A
2018-01-19-12-06-49_S2_27QTU	19/01/18 12:06	2.9	19.33	20.94	6.8	A
2020-02-18-12-07-03_S2_27QTU	18/02/20 12:07	2.57	19.39	359.46	7.1	A
2017-02-17-11-57-30_L8_210048	17/02/17 11:57	2.48	20.26	342.71	2.5	A
2022-11-07-11-52-25_L8_209049	07/11/22 11:52	2.31	18.49	344.16	7.6	A
2017-11-09-11-52-03_L8_209049	09/11/17 11:52	1.8	18.07	358.61	8.0	A
2016-01-10-12-07-14_S2_27QTU	10/01/16 12:07	1.77	19.24	356.6	7.2	A
2022-12-04-12-07-09_S2_27QTU	04/12/22 12:07	1.28	18.73	343.33	7.2	A
2018-02-28-12-06-52_S2_27QTU	28/02/18 12:06	4.61	18.67	327.63	6.9	R
2018-03-01-11-51-05_L8_209048	01/03/18 11:51	4.39	16.38	327.71	8.9	R
2017-03-30-11-51-22_L8_209049	30/03/17 11:51	3.77	18.07	344.08	8.6	R
2017-03-30-11-50-58_L8_209048	30/03/17 11:50	3.77	18.07	344.08	9.0	R
2021-01-11-11-57-46_L8_210048	11/01/21 11:57	3.69	9.48	38.37	2.2	R
2021-01-11-12-17-03_S2_27QTU	11/01/21 12:17	3.69	9.48	38.37	17.1	R
2016-02-15-11-57-30_L8_210048	15/02/16 11:57	3.65	9.74	24.85	2.5	R
2019-12-17-11-52-04_L8_209049	17/12/19 11:52	3.65	17.57	6.11	7.9	R
2019-12-17-11-51-40_L8_209048	17/12/19 11:51	3.65	17.57	6.11	8.3	R
2014-01-08-11-58-51_L8_210048	08/01/14 11:58	3.55	16.78	335.1	1.2	R
2015-02-21-11-51-36_L8_209049	21/02/15 11:51	3.51	9.77	25.35	8.4	R
2015-02-21-11-51-12_L8_209048	21/02/15 11:51	3.51	9.77	25.35	8.8	R
2022-03-02-12-17-08_S2_27QTU	02/03/22 12:17	3.48	16.01	15.62	17.1	R

PALEO EXTREME WAVES ON SAL ISLAND, CAPE VERDE ARCHIPELAGO.

2022-03-12-11-51-21_L8_209048	12/03/22 11:51	2.98	19.37	5.46	8.7	R	
2018-01-19-11-57-35_L8_210048	19/01/18 11:57	2.9	19.33	20.94	2.4	R	
2022-11-07-11-52-01_L8_209048	07/11/22 11:52	2.31	18.49	344.16	8.0	R	
2022-03-20-11-51-47_L9_209049	20/03/22 11:51	2.31	18.2	8.53	8.2	R	
2022-03-20-11-51-23_L9_209048	20/03/22 11:51	2.31	18.2	8.53	8.6	R	
2018-02-21-12-16-48_S2_27QTU	21/02/18 12:16	1.86	19.47	11.14	16.8	R	
2017-11-09-11-51-40_L8_209048	09/11/17 11:51	1.8	18.07	358.61	8.3	R	
2014-10-16-11-52-01_L8_209049	16/10/14 11:52	1.39	18.98	17.77	8.0	R	
2014-10-16-11-51-37_L8_209048	16/10/14 11:51	1.39	18.98	17.77	8.4	R	
2019-10-26-12-07-10_S2_27QTU	26/10/19 12:07	1.08	18.53	18.25	7.2	R	

Supplementary Table 2. Main dimensions (a-, b-, and c-axes), calculated volume, estimated mass, and assumed lithological density for the seven boulders surveyed in the study area. Volumes were derived from 3D models generated via Structure-from-Motion/Multi-View Stereo (SfM/MVS), and masses were calculated based on measured volume and estimated rock density.

Boulder ID	A axis (m)	B axis (m)	C axis (m)	Actual Volume (m³)	Actual Mass (t)	Density (kg/m³)
1	4.2	3.5	1.3	13.6	31.3	2300
2	3.8	2.0	1.5	8.9	22.3	2500
3	5.7	3.1	1.9	17.8	44.4	2500
4	4.0	3.1	2.5	16.4	40.9	2500
5	2.1	1.7	1.5	3.0	8.5	2800
6	5.7	3.2	1.5	25.3	58.2	2300
7	2.1	1.5	1.1	1.2	3.3	2800

Supplementary Table 3. Threshold flow velocities (in m/s) required to initiate movement of the seven boulders surveyed in the study area, based on the empirical formulations of Nandasena et al. (2022). Values are shown for both submerged/sub-aerial isolated boulders and joint-bounded boulders, and include thresholds for sliding, overturning, and saltation/lift for joint-bounded boulders.

	Submerg	Joint bounded		
Boulder ID	Sliding	Overturning	Saltation	Saltation/Lift
1	3.8	7.2	10.9	11.04
2	3.8	6.0	13.9	14.10
3	3.9	6.5	13.8	14.00
4	3.8	5.7	14.2	14.32
5	3.4	5.0	15.6	15.79
6	4.2	7.5	13.5	13.68
7	2.4	3.8	8.7	8.80